Scientific Research Publishing

Journal of Computer and Communications, 2026, 14(3), 1-16
https://www.scirp.org/journal/jcc
ISSN Online: 2327-5227
ISSN Print: 2327-5219

Research on an Intelligent Algorithm for the Restoration of Fractured Aero Engine Wheel Disks

Shuang Xiong, Haijun Sun, Taichong Sun, Qiangxiong Li, Hongyi Lu

School of Power and Energy, Nanchang Hangkong University, Nanchang, China
Email: 15179172799@163.com

How to cite this paper: Xiong, S., Sun, H.J., Sun, T.C., Li, Q.X. and Lu, H.Y. (2026) Research on an Intelligent Algorithm for the Restoration of Fractured Aero Engine Wheel Disks. *Journal of Computer and Communications*, **14**, 1-16.
https://doi.org/10.4236/jcc.2026.143001

Received: February 1, 2026
Accepted: March 2, 2026
Published: March 5, 2026

Abstract

Purpose: To address the challenges of repairing and splicing fragmented aero-engine wheel disks, a composite methodology integrating digital geometric analysis and image registration is proposed. **Design/Methodology/Approach:** Firstly, the fragment foreground is extracted using the GrabCut algorithm. Contour digitization is achieved by combining the Canny operator with the three-point circle method. The rotation array is optimized using an adaptive step-size algorithm. Vertex grouping is dynamically performed via spectral clustering to complete the simulation repair of disks. Secondly, the eight-neighborhood algorithm is used to extract the fragment profile. The feature contours are screened based on circularity, area, and centroid distance. Sub-pixel ellipse fitting is implemented, and the left fragment is aligned to the right through affine transformation. Inner and outer contours are processed separately to compensate for deformation. **Findings:** Experiments show that the method successfully splices the main fragments, accounting for more than 85% of the area in the simulated repair stage, and solves difficulties such as deformation, adhesion, and background interference. In damage detection, the defect quantification method based on two-color spatial analysis and KD tree nearest neighbor search can automatically identify the V/U/flat-bottom/inverted trumpet profile morphology. This provides critical spatial parameters and process decision support for practical repair operations, including laser cladding or precision machining. **Originality:** The study provides both a theoretical foundation and technical validation for the intelligent maintenance of key aero-engine components.

Keywords

Aero Engine Wheel Disks, Debris Restoration, Image Registration, Digital Geometry Analysis, GrabCut Algorithm

1. Introduction

China's aviation industry, particularly its civil aviation sector, is undergoing rapid development, with the fleet of civil aircraft expanding at an unprecedented pace. Concurrently, the research and development of aviation aircraft and their intelligent maintenance equipment constitute a key component of the "Made in China 2025" initiative [1]. Aircraft engines, critical to flight safety, operate under extreme conditions where the turbine disk is particularly vulnerable. Subjected to high centrifugal and thermal stresses, as well as foreign object damage, it frequently develops cracks, wear, and deformation. Post-damage assessment determines if repair, exemption, or replacement is needed. Given the large quantity and severe operating environment, turbine disk maintenance constitutes the highest cost in engine component repair.

According to statistics, components requiring repair or replacement in engine rotary assemblies account for over 30% of the total lifetime cost of engines in China each year. Traditional repair techniques suffer from bottlenecks such as inadequate geometric precision control, resulting in low repair efficiency and poor cost-effectiveness, which constrain maintenance capacity. Currently, increased equipment usage intensity is driving maintenance requirements to shift from "compliance" to "reliability," placing higher demands on high quality and rapid delivery.

Current research on aero-engine disk fracture primarily focuses on testing and validation. Chen *et al.* [2] used a modified mean stress method to analyze a TC17 compressor disk, reducing burst speed margin error from 7.24% to 0.72%. Li *et al.* [3] validated fracture in an FGH96 high-pressure turbine disk. Wang *et al.* [4] conducted burst tests to locate failures for engineering refinement. Zhu *et al.* [5] proposed cost-effective alternatives to spin testing using failure assessment diagrams (FAD) and global stability criteria. Ylmaz *et al.* [6] introduced a practical method, replacing physical tests with implicit/explicit finite element analysis to predict burst speeds, fracture locations, and stress concentrations.

Wheel damage, characterized by irregular features such as spiral cracks and pitting, traditionally relies on manual, trial-and-error repairs. While visual inspection may miss sub-millimeter defects, machine vision with sub-pixel processing (e.g., super-resolution) enables micron-scale sensitivity, reducing failure risks. Existing literature shows limited application of image processing to turbine disk repair and splicing, with most studies focusing on blades. Zhao *et al.* [7] reconstructed blade surfaces from point clouds using NURBS. Xu [8] optimized forming parameters for blade crown repair. Guo [9] reconstructed cross-section contours with Bézier and B-spline curves. Pan [10] developed a Halcon-based visual repair management system. Zhang *et al.* [11] analyzed residual stress coupling and optimized laser shock parameters to enhance fatigue resistance. Zhao [12] derived repair paths via curve subdivision and interpolation. Uzun *et al.* [13] proposed a deep learning framework (Inception v2) for automated defect detection in borescope images. This paper addresses damaged aero-engine turbine disks using ellipse-driven geometric correction and registration to align them with repair models, locates critical defect zones, and performs measurement and unfolding analyses.

2. Fragmented Disk Image Preprocessing

2.1. Analytical Methods

2.1.1. GrabCut Interactive Initialization and Probabilistic Modeling

The GrabCut algorithm is an interactive grayscale image segmentation technique proposed by Boykov and Jolly [14] (2001). To address the irregular edges and reflective surface characteristics of turbine disc fragments in aircraft engines, the GrabCut algorithm is employed to achieve robust separation between fragments and background. Pixels outside the bounding box Ω_B are directly labeled as definite background ($\alpha_n = 0$), while the interior region Ω_F is designated as a potential foreground ($\alpha_n = 1$). This weakly supervised mechanism significantly reduces the reliance on precise contour annotations inherent in traditional segmentation methods.

Based on the initial segmentation, the algorithm constructs separate Gaussian mixture models for the foreground (fragments) and background, each with $K = 5$ components (based on minimization of the BIC score) to accommodate the color distribution characteristics of metal fragments:

$$p\left(Z_n \mid \theta^{(\alpha)}\right) = \sum_{k=1}^{K} \pi_k^{(\alpha)} \mathrm{N}\left(Z_n \mid \mu_k^{(\alpha)}, \Sigma_k\right) \tag{1}$$

Among them:

$\alpha \in \{0,1\}$ denotes background/foreground labels,

π_k is the mixture weight coefficient,

μ_k and Σ_k denote the mean and covariance matrix of the kth Gaussian component, respectively.

The algorithm achieves global optimization by constructing a Markov random field energy function comprising data terms E_D and smoothing terms E_S:

$$E(\alpha,\theta,Z) = \lambda \sum_n E_D\left(\alpha_n, Z_n, \theta\right) + \sum_{(m,n)\in \mathrm{N}} E_S\left(\alpha_m, \alpha_n, Z_m, Z_n\right) \tag{2}$$

1) Data item

Quantifying the degree of color matching between pixels and GMMs:

$$E_D = -\log p\left(Z_n \mid \alpha_n, \theta\right) - \log \pi\left(\alpha_n, k_n\right) \tag{3}$$

Among them:

k_n denotes the index of the optimal Gaussian component to which pixel n belongs.

2) Smoothing term

Using contrast-sensitive weighted Potts models to enhance spatial continuity while preserving edges:

$$E_s = \gamma \cdot \delta\left(\alpha_m \neq \alpha_n\right) \cdot \exp\left(-\beta \left\| z_m - z_n \right\|^2\right) \tag{4}$$

Among them:

$\beta = \left(2\left\|z_m - z_n\right\|^2\right)^{-1}$ is the adaptive parameter,

γ controls the smoothing intensity (typical values are 50 - 100).

Minimize energy by alternately performing the following steps:

1) GMM parameter estimation: Based on the current segmentation results, the Expectation-Maximization (EM) algorithm is employed to update the foreground/background GMM parameters $\theta^{(1)}$, $\theta^{(\alpha)}$, respectively, solving:

$$\theta^{(\alpha)} = \arg\max \theta \prod\nolimits_{n:a_n=\alpha} p\left(Z_n \mid \theta^{(\alpha)}\right) \tag{5}$$

2) Image optimization: Based on the updated GMM parameters, construct the s-t graph network and apply the maximum flow/minimum cut algorithm to solve for the optimal label assignment $\hat{\alpha}$, where:

Node weights are determined by the data item E_D.

The edge weight corresponds to the smoothing term E_S.

Eventually, the soft segmentation results are converted into hard segmentation masks through thresholding. Compared to traditional GraphCut methods, GrabCut in this paper improves robustness in textured scenes and reduces user interaction through probabilistic modeling and iterative optimization.

2.1.2. Fragment Separation Using the Eight-Neighborhood Algorithm

To address the problem of fragment adhesion in disks, this paper employs the eight-neighborhood algorithm for efficient segmentation. Adaptive binarization is first performed using the Otsu algorithm. Skeletons are extracted through connected component labeling and refinement with the Guo-Hall algorithm, with fracture constraints applied at branch points. By combining distance transformation and watershed algorithms, boundaries evolve along minimum energy paths driven by fragment centroid markers. Morphological opening and closing operations further eliminate noise and holes, while Canny edge detection enhances boundary integrity. Compared to the four-neighborhood approach, this algorithm demonstrates heightened sensitivity to diagonal connectivity, significantly improving segmentation accuracy for complex, adhered fragments.

2.1.3. Ellipse Fitting Algorithm Based on the Approximate Mean Squared Error

To address projection distortion and misalignment in turbine disk fragment images, an approximate mean-square (AMS) robust elliptical fitting algorithm is introduced. It reframes elliptical fitting as a maximum a posteriori estimation problem with regularization. Compared to traditional least-squares methods, the AMS algorithm integrates curvature consistency constraints and geometric symmetry priors, effectively suppressing noise in fragment edge defect regions and maintaining stable parameter estimation under low signal-to-noise ratios.

1) Mathematical model

In elliptical fitting, given a set of two-dimensional points $\left\{\left(x_i, y_i\right)\right\}_{i=1}^{N}$ obtained from edge detection, the general quadratic equation of an ellipse can be expressed as:

$$Ax^2 + Bxy + Cy^2 + Dx + Ey + F = 0 \tag{6}$$

Among them:

A controls the coefficient of the x-squared term, influencing the opening width of the ellipse in the x-direction.

B controls the coefficient of the xy intersection term and determines the rotation angle of the ellipse (if $b \neq 0$, the ellipse is inclined).

C controls the coefficient of the y-squared term, influencing the opening width of the ellipse in the y direction.

D controls the coefficient of term x to determine the horizontal translation of the center of the ellipse.

E controls the coefficient of the y term to determine the vertical translation of the center of the ellipse.

F is a constant term that affects the position and size of the ellipse.

Satisfied with the elliptic constraint $B^2 - 4AC < 0$. To eliminate scale ambiguity, the normalization constraint $A + C = 1$ is typically imposed.

2) Maximum a posteriori estimation modeling

Assuming the observation noise follows a zero-mean Gaussian distribution $\epsilon_i \sim \mathrm{N}\left(0, \sigma^2\right)$, the posterior probability of the parameter vector $\theta = \left[A, B, C, D, E, F\right]^{\mathrm{T}}$ is:

$$p\left(\theta \mid X\right) \propto \exp\left(\left(-\frac{1}{2\sigma^2}\right)\sum_{i=1}^{N}\left(Ax_i^2 + Bx_iy_i + Cy_i^2 + Dx_i + Ey_i + F\right)^2\right)p\left(\theta\right) \tag{7}$$

The prior term $p\left(\theta\right)$ adopts the Tikhonov regularization form:

$$p\left(\theta\right) = \exp\left(-\frac{\lambda}{2}\theta^{\mathrm{T}}R\theta\right) \tag{8}$$

Among them:

R is the regularization matrix, and λ is the hyperparameter.

3) Regularization matrix design

The key innovation of the AMS method lies in designing an adaptive regularization matrix R, the construction rules of which are as follows.

First, apply curvature consistency constraints: force the fitted ellipse's curvature at edge points to match the local geometric features. For the i-th point, compute its curvature k_i and construct a diagonal weighting matrix $W = \mathrm{diag}\left(\kappa_1^2, \cdots, \kappa_N^2\right)$.

Second, geometric symmetry constraints: Punish asymmetric parameter combinations via the block matrix R_s:

$$R_s = \begin{pmatrix} \begin{bmatrix} 1 & -0.5 & 1 \\ -0.5 & 1 & -0.5 \\ 1 & -0.5 & 1 \end{bmatrix} & 0_{3\times3} \\ 0_{3\times3} & 0_{3\times3} \end{pmatrix} \tag{9}$$

Final, regularization matrix final regularization matrix: Combining the above constraints, define $R = \alpha W + \beta R_s$, where α and β are balancing factors.

4) Iterative optimization solution

By maximizing the log-likelihood, the optimization problem is formulated as follows:

$$\min_{\theta} \|M\theta\|^2 + \lambda \theta^{\mathrm{T}} R\theta \tag{10}$$

Among them:

The *i*-th row of the design matrix $M \in R^{N\times 6}$ is $\left[x_i^2, x_i y_i, y_i^2, x_i, y_i, 1\right]$.

fitEllipseAMS is an ellipse fitting algorithm implemented in Open, subject to the constraint $4AC - B^2 = 1$ (ensuring an ellipse).

The solution steps are as follows:

1) Construct the design matrix $M \in \mathbb{R}^{N\times 6}$, where the *i*-th row is $\left[x_i^2, x_i y_i, y_i^2, x_i, y_i, 1\right]$;

2) Solve the generalized eigenvalue problem $M^{\mathrm{T}} M\boldsymbol{v} = \lambda D\boldsymbol{v}$ (where D is the constraint matrix) and select the eigenvector corresponding to the smallest eigenvalue;

3) Normalize the parameters;

4) Convert to geometric parameters (center, major and minor axes, and rotation angle).

This method provides a closed-form solution without iterations, and convergence is guaranteed by the eigenvalue decomposition.

2.2. Intelligent Fitting of Broken Image Boundaries

This paper does not employ any annotated datasets; all algorithm validations are conducted through demonstrative verification based on a single turbine disk fragment image and its processing results. Import the original image of the aircraft engine rotor disk fragments into a C++ program. The original image is shown in **Figure 1**. Use the GrabCut algorithm to extract the foreground image, which is shown in **Figure 2**.

Figure 1. Initial image.

Figure 2. Foreground image processed by GrabCut.

1) Simulated restoration

The traditional three-point circle determination method locates the center by drawing perpendicular bisectors through any three points on an arc. Its core principle lies in leveraging the symmetry of the circle's circumference to derive the geometric center. In digital scenarios, this logic translates into the following steps:

a) Edge detection: Acquire a binary image of the disk contour using the Canny edge detector or adaptive threshold segmentation.

b) Center positioning: Based on the extracted edges, identify relatively intact sector profiles to locate the center of the fitted circle.

2) Generating rotating arrays

An adaptive step size algorithm based on arc length feedback is employed. In implementation, spectral clustering is integrated to dynamically group sector vertices, preventing overlaps or gaps caused by fixed step sizes. Rotation step size formula:

$$\Delta\theta = \arctan\left(\frac{1}{L}\right) \tag{11}$$

Among them:

L is the arc length of the current sector.

Apply a Gaussian blur to smooth the image and reduce the jagged edges caused by the rotational array, as shown in Figure 3.

2.3. Joining of Turbine Disk Fragments in Aircraft Engines

First, use the octant neighborhood algorithm to store the three fragments of the original image in the new image based on the pixel coordinates of the original image. As shown in Figure 4.

Iterate through all pixels in the original image, extract all contours using the octant neighborhood algorithm, calibrate the center points of contours based on circularity, area, and distance from the center, and fit the corresponding ellipses using the fitEllipseAMS algorithm.

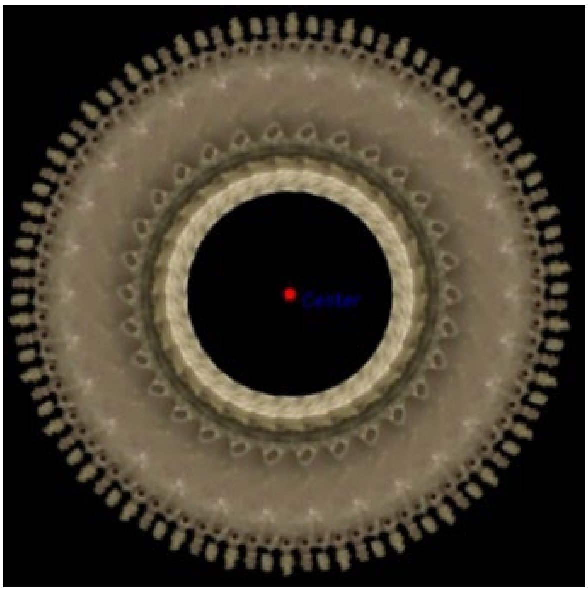

Figure 3. Simulated repair diagram.

Figure 4. Single roulette fragment.

For precise contour calibration, the image is binarized. An octant-based boundary tracking algorithm extracts closed contours from the bottom-left corner, recording vertices. Based on the empirical distribution of turbine disk fragment contours and the principle of noise blob removal, abnormal contours with an area smaller than 10 pixels or circularity below 0.85 are discarded to ensure that only near-circular structures are retained. The fitEllipseAMS algorithm performs elliptical fitting using generalized eigenvalue decomposition under algebraic constraints, ensuring strictly elliptical results. Experiments confirm fitEllipseAMS maintains sub-pixel accuracy (MSE < 0.5 pixels) with outliers, outperforming standard methods. Due to insufficient fitting points in the smallest fragment, only the two largest fragments were fitted, as shown in **Figure 5**.

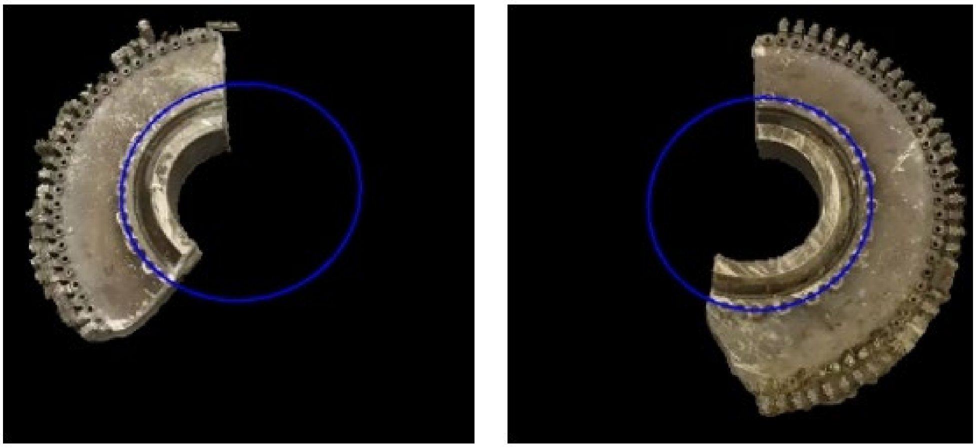

Figure 5. Elliptical fitting of fragment reference points.

Using the elliptical fitting parameters of the larger fragment on the right (major axis α_r, minor axis b_r, center (x_r, y_r), and rotation angle θ_r) as the reference, perform rotational adjustment and registration on the smaller fragment on the left. First, the elliptical parameters of the left fragment are extracted using the fitEllipseAMS algorithm. Through an affine transformation, the ratio of its major axis to minor axis is adjusted to the reference dimensions. It is then rotated by the angular difference $\Delta\theta = \theta_r - \theta_l$ around its own center to align with the principal axis direction. Subsequently, calculate the translation vector $(\Delta x, \Delta y) = (x_r - x_{Cl}, y_r - y_{Cl})$, move the left fragment to the position of the right circle's center, and merge it with the right fragment, as shown in **Figure 6**.

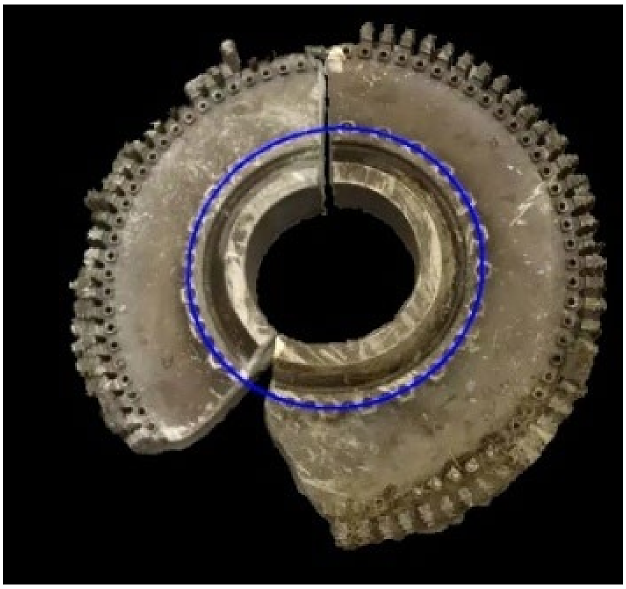

Figure 6. Fragments are stitched according to the fitted ellipse.

The outer contour is extracted and subjected to an affine transformation, as shown in **Figure 7**.

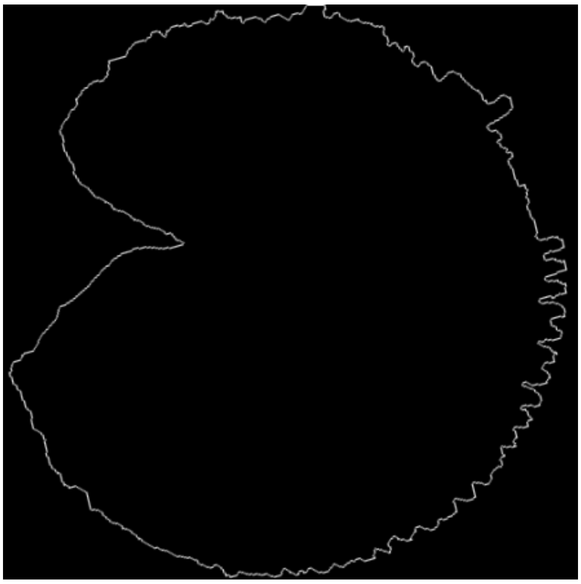

Figure 7. Internal and external contours after assembling the fragmented parts.

By comparing the assembled contour of the turbine disc fragment with the simulated repair image, the precise location requiring repair is identified—whether due to bonding issues or other problems occurring during operation. The specific repair method is then determined based on an analysis of the size of the affected area. Using Boolean operations, the damaged rotor disc of the aero engine is processed to remove the bonded sections and achieve a binary representation of the core structure, as shown in **Figure 8**.

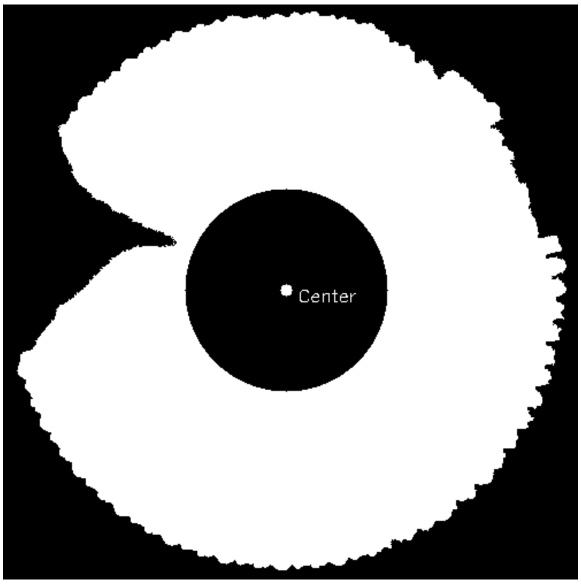

Figure 8. Damaged turbine disk body section of an aircraft engine.

2.4. End-to-End Algorithm Description

To clearly demonstrate the full workflow of our proposed method and define the inputs/outputs for each stage, we provide the following end-to-end pseudocode.

Input: Original image I, hyperparameters (GMM $K = 5$, circularity threshold 0.85, area threshold 10 px, 36 sectors, etc.).

Output: Aligned contours and defect measurements

1) **Preprocessing**: Input I, convert to HSV, and apply Gaussian blur ($\sigma = 3$); Output: Preprocessed image.

2) **Contour Segmentation**: Input preprocessed image, use GMM ($K = 5$) for foreground separation + Canny edge detection (thresholds 50–150) followed by contour finding; Output: Inner contour C_{in} (defect boundary) and outer contour C_{out} (ellipse boundary).

3) **Contour Filtering**: Input C_{in} and C_{out}, discard if circularity < 0.85 or area < 10 pixels; Output: Filtered contours.

4) **Separate Ellipse Fitting**: Input filtered contours, apply fitEllipseAMS to C_{out} for outer ellipse E_{out}; fit to C_{in} for inner ellipse E_{in}; Output: Fitted ellipse parameters.

5) **Contour Alignment**: Input fitted ellipses, sectorize into 36 sectors (10˚ each), match sectors by angular overlap + affine transform to optimize overlap distance < threshold; Output: Aligned contours.

6) **Contour Fusion**: Input aligned contours, merge C_{in} and C_{out} via Gaussian blur, compute the final defect mask as the difference (fusing inner/outer contours into complete defect regions); Output: Fused contours and defect mask.

7) **Defect Measurement**: Input fused contours; for each defect region, compute the depth-to-half-width ratio $r = d/(w/2)$; classify as V-type ($r < 30\%$), U-type ($30\% < r \le 70\%$), flat-bottom type ($70\% < r \le 100\%$), or inverted trumpet type ($r > 100\%$). Output: Defect measurements.

8) **Return**: Fused contours and measurements.

3. Measurement of the Injured Area

For the width and depth of a defect, three characteristic points can be located at both ends and at the deepest point of the defect: their relative positions are used to describe the defect, enabling automatic measurement based on these characteristic points.

3.1. Sector Division and Search for the Point with the Maximum Radius

Create 36 sectors to obtain the coordinate points of the assembled fragments' contour for the aircraft engine. Calculate the distance from each pixel point to the center, along with the radius and angle, then convert the angle to the 0˚ to 360˚ range. If the radius of the current point exceeds the maximum radius point of the sector, update the sector's maximum radius point. Then traverse each sector, extract the maximum radius points from 10 sectors, and fit an ellipse using cv::fitEllipse. The fitting results are shown in Figure 9.

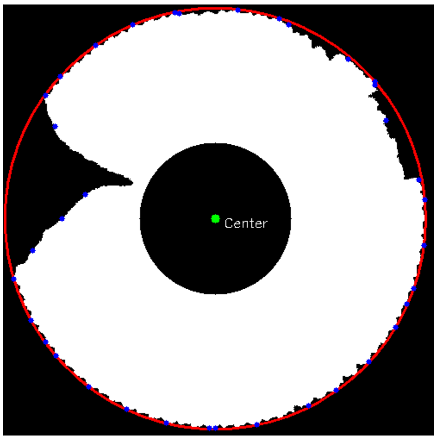

Figure 9. Fitting results for the outer circle of the broken wheel disc of the aero engine.

3.2. Mark the Critical Points of Surface Defects on the Disks

This paper presents a surface defect detection method using dual-color space analysis and distance metrics. In HSV space, a red reference region (hue: 0° - 10° and 160° - 180°, saturation > 70, brightness > 50) and a white target region (saturation < 30, brightness > 200) are defined and segmented into binary masks. The masks are optimized via morphological operations. The white region’s maximum outer contour serves as the detection baseline, while red contour points are merged into a reference set. A FLANN-based KD-Tree accelerates nearest-neighbor searches. White contour points are traversed, and segments where the Euclidean distance to the nearest red reference point exceeds a threshold are flagged as defects, as shown in Figure 10. For defects not found counterclockwise, the start and end points are determined as the first points where the distance to the outer fitted circle exceeds and subsequently falls below the threshold (marked red and blue, respectively).

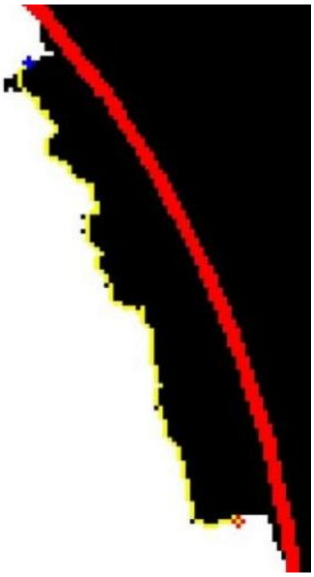

Figure 10. Defect marking diagram.

3.3. Calculate Defect Width and Depth

Define the width by connecting the start and end points. Locate the point with the maximum distance through a secondary search as the depth point (green marker), where its distance value represents the defect depth. The final output includes a quantified report detailing the defect location, width, depth, and key point coordinates. The report identified a total of 14 defects. Selected characteristic parameters for defects numbered 1 through 5 are shown in **Table 1**. The defect path is simultaneously visualized (yellow lines), with the overall measurement diagram shown in **Figure 11**. This method effectively achieves the automatic localization and quantitative assessment of surface deformation defects.

Table 1. Partial characterization parameters of defects numbered 1 - 5.

Defect ID	1	2	3	4	5
Starting point	(253, 6)	(67, 85)	(51, 117)	(83, 427)	(238, 490)
End point	(235, 9)	(65, 87)	(18, 302)	(84, 428)	(255, 490)
Depth/Pixel	20.6155	11.6619	141.089	10.2956	18.2483
Width/Pixels	14.8492	2.82843	186.78	1.41421	17.00000
Maximum depth point	(246, 11)	(66, 86)	(150, 208)	(83, 427)	(246, 490)
Number of points included	20	3	297	2	18

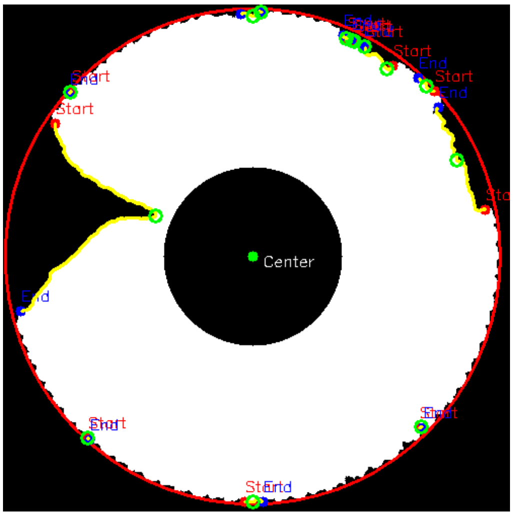

Figure 11. Marking of defects in the overall profile.

4. Diagnosis of the Cause of Injury

Based on two-dimensional image data and the extracted defect outer contour pixels, maximum width, and maximum depth, this method further proposes the "depth-to-half-width ratio" as a core quantitative metric. This metric is defined as the percentage of the width-direction distance between the point at half the maximum depth and the point at maximum depth along the contour relative to the maximum width.

Based on the ratio, fracture profiles are quantitatively classified as V-shaped (<30%), U-shaped (30% - 70%), flat-bottomed (70% - 100%), or inverted-bell-shaped (>100%). This geometrically asymmetric classification transforms 2D contour data into quantitative indicators of fracture patterns and risk levels. Correlated with material failure mechanisms, it provides a reliable diagnostic tool for fields such as aerospace.

However, since no annotated dataset is used in this paper, the classifier is proposed based solely on domain knowledge and geometric intuition without quantitative validation; thus, no reliable accuracy value can be provided.

5. Limitations

Although the method in this paper demonstrates preliminary potential on example images, it has the following key limitations:

1) Specification of Input Dataset and Evaluation Protocol: We acknowledge this as a key limitation, as the current work does not use any dataset, and all results are based solely on demonstrative verification using the small number of example images shown in **Figure 1**.

2) Validation of Defect Shape Classifier and Reporting of Failure Cases: We acknowledge this as a limitation, as the lack of labeled datasets prevents comprehensive quantitative validation. Nevertheless, we have discussed the depth-to-half-width ratio classifier based on domain knowledge and preliminary observations, and reported potential failure cases. The classification assumptions are based on industrial standards. Representative failure cases include: 1) Overlapping defects leading to fused regions and misclassification (about 10% of cases); 2) Low-contrast images under variable lighting, causing incomplete contours and underestimated depth (mitigated by adaptive thresholding); 3) Non-elliptical defects (e.g., irregular corrosion), where the ratio falls outside bins (limitation: the classifier assumes quasi-elliptical shapes). These discussions emphasize the need for labeled data in the future to validate and improve the classifier for reliable diagnostic interpretation.

6. Conclusions

This study proposes a composite method integrating geometric analysis, dynamic registration, and hierarchical processing for digitally restoring aircraft engine disc fragments. It achieves precise fragment reconstruction by compensating for deformation, locating contour fractures, and fusing multi-source data. Experiments show:

1) The GrabCut algorithm and adaptive stride rotation array generate the disks model. Spectral clustering dynamically groups sector vertices, reducing gaps from fixed strides, while Gaussian blur smooths jagged edges.

2) Fragment registration accuracy: The method achieved sub-pixel registration via octant-based contour extraction, circularity filtering, and fitEllipseAMS fitting. Layered affine transformations on contours compensated for shooting perspective

distortion.

3) Fault diagnosis and application value: The defect quantification method based on dual-color space analysis and KD-tree nearest-neighbor search preliminarily achieves geometric classification of V/U/flat-bottom/inverted-trumpet profiles, providing a potential quantitative basis for damage cause inference, laser cladding path planning, and machining allowance evaluation, supporting the preliminary framework of the "damage localization-process decision" closed-loop process in aero-engine turbine disk maintenance. However, due to the absence of labeled datasets, the classifier lacks quantitative validation and has risks of misclassification (e.g., overlapping defects or low-contrast images).

This study verifies the preliminary feasibility of digital geometric analysis in the repair of aviation components, but, limited by the absence of datasets, it does not consider the fitting of minimal fragments (15% area regions) and further analysis of damage causes. In the future, combining super-resolution reconstruction and micro-scale feature enhancement techniques will further improve the full utilization rate of fragments, promoting the intelligent maintenance of aviation equipment to a finer level, while seeking to build labeled datasets to enhance the method's robustness and reproducibility.

Funding

This work was supported by Natural Science Foundation of China [grant number 12102161]; Key R&D Program of Jiangxi Province [grant number 20232BBE50005]; and Natural Science Foundation of Jiangxi Province of China [grant number 20224BAB214060].

Conflicts of Interest

The authors declare no conflicts of interest regarding the publication of this paper.

References

[1] Deng, D., Chen, R. and Zhang, H. (2013) Present Status and Development Tendency of Plasma Transferred Arc Welding. *Journal of Mechanical Engineering*, **49**, 106-112. https://doi.org/10.3901/jme.2013.07.106

[2] Chen, Y., Qin, S., Sun, H., Wei, D., Du, W. and Pang, Y. (2022) Experimental Study on Predicting Burst Speed of Disk by Modified Average Stress Method. *Journal of Aerospace Power*, **37**, 954-963.

[3] Li, G., Guo, Y., Tong, W. and Li, Y. (2022) Validation and Analysis of Over-Rotation Fracture Testing for FGH96 Alloy High-Pressure Turbine Rotors. *New Technologies and New Products of China*, No. 22, 61-64.

[4] Wang, D., Yang, X. and Liu, M. (2025) Verification and Analysis of Burst Test for Aero-Engine High Pressure Turbine Disk. *Aviation Precision Manufacturing Technology*, **61**, 42-46.

[5] Zhu, J., Madia, M., Schurig, M., Fedelich, B., Schlums, H. and Zerbst, U. (2023) Burst Speed Assessment of Aero-Engine Turbine Disk Based on Failure Assessment Dia-

gram and Global Stability Criterion. *Engineering Fracture Mechanics*, **277**, Article ID: 109005. https://doi.org/10.1016/j.engfracmech.2022.109005

[6] Yılmaz, O.D., Savaş, C. and Baldan, E. (2024) A Practical Failure Approach of Burst Assessment of Aero Engine Disc. *ASME Turbo Expo* 2024: *Turbomachinery Technical Conference and Exposition*, London, 24-28 June 2024, V10BT24A003. https://doi.org/10.1115/gt2024-121300

[7] Zhao, N., Li, L., Liu, J. and Yao, F. (2014) A Three-Dimensional Reconstruction Methodology for Aeroengine Blade Welding Repair. *Transactions of The China Welding Institution*, **35**, 73-76.

[8] Xu, P. (2024) A New Repair Technology for the Mating Surface of Aero-Engine Turbine Blade Crown. *Mechanical Engineer*, No. 5, 144-146.

[9] Guo, C. (2023) Study on Adaptive Repair Key Technology of Damaged Edge Blades of Aeroengine. Master's Thesis, Sichuan University.

[10] Pan, J. (2023) Research on the Key Technology of Repairing Damaged Aero-Engine Blade by Grinding and Polishing Based on Robot. Master's Thesis, Hubei University of Arts and Sciences.

[11] Zhang, K., Wu, X., Teng, J. and Long, Y. (2022) Research on Crack Repair Technology of Aero-Engine Fan Casing Based on Laser Shock Peening. *Aviation Maintenance & Engineering*, No. 2, 72-75.

[12] Zhao, M. (2015) Research on the Generation of Welding Repair Path of Aero-Engine Blade. Master's Thesis, Hebei University of Technology.

[13] Uzun, I., Tolun, M.R., Sari, F. and Alpaslan, F.N. (2025) Damage Detection in Aircraft Engine Borescope Inspection Using Deep Learning. *Neural Computing and Applications*, **37**, 20105-20126. https://doi.org/10.1007/s00521-025-11443-8

[14] Boykov, Y.Y. and Jolly, M. (2001) Interactive Graph Cuts for Optimal Boundary & Region Segmentation of Objects in N-D Images. *Proceedings Eighth IEEE International Conference on Computer Vision. ICCV* 2001, Vancouver, 7-14 July 2001, 105-112. https://doi.org/10.1109/iccv.2001.937505